



OPEN

# Reduction of dopant ions and enhancement of magnetic properties by UV irradiation in Ce-doped TiO<sub>2</sub>

Tai-Sing Wu<sup>1</sup>, Leng-You Syu<sup>2</sup>, Bi-Hsuan Lin<sup>1</sup>, Shih-Chang Weng<sup>1</sup>, Horng-Tay Jeng<sup>2,3</sup>, Yu-Shan Huang<sup>1</sup> & Yun-Liang Soo<sup>1,2</sup>✉

We report the experimental observation of and theoretical explanation for the reduction of dopant ions and enhancement of magnetic properties in Ce-doped TiO<sub>2</sub> diluted magnetic semiconductors from UV-light irradiation. Substantial increase in Ce<sup>3+</sup> concentration and creation of oxygen vacancy defects in the sample due to UV-light irradiation was observed by X-ray and optical methods. Magnetic measurements demonstrate a combination of paramagnetism and ferromagnetism up to room temperatures in all samples. The magnetization of both paramagnetic and ferromagnetic components was observed to be dramatically enhanced in the irradiated sample. First-principle theoretical calculations show that valence holes created by UV irradiation can substantially lower the formation energy of oxygen vacancies. While the electron spin densities for defect states near oxygen vacancies in pure TiO<sub>2</sub> are in antiferromagnetic orientation, they are in ferromagnetic orientations in Ce-doped TiO<sub>2</sub>. Therefore, the ferromagnetically-oriented spin densities near oxygen vacancies created by UV irradiation are the most probable cause for the experimentally observed enhancement of magnetism in the irradiated Ce-doped TiO<sub>2</sub>.

Titanium-dioxide-based diluted magnetic semiconductors (DMS) have been widely considered as promising ferromagnetic material possibly useful for spintronic applications. The structures, electronic states, and magnetic properties in transitional metal-doped TiO<sub>2</sub> have been previously studied<sup>1–4</sup>. However, despite reports of successful materials synthesis and favorable magnetic properties, questions remain regarding the origin of the materials' magnetism and consequently their applicability in spintronics<sup>5</sup>. On the other hand, it is possible that the intrinsically non-magnetic CeO<sub>2</sub> may undergo magnetic phase transition when oxygen vacancy defects (V<sub>O</sub>) are introduced to the material. As reported in a recent paper, UV-irradiated CeO<sub>2</sub> indeed demonstrates enhanced room-temperature ferromagnetism<sup>6</sup>. UV irradiation is thought to generate oxygen vacancies, converting a substantial fraction of constituent Ce<sup>4+</sup> into subvalent Ce<sup>3+</sup> and thus enhancing ferromagnetic ordering in the ceria sample. It is therefore conceivable that a new species of TiO<sub>2</sub>-based DMS may be obtained by doping Ce into titanium dioxide hosts followed by UV irradiation.

In the present work, we have used rare-earth element Ce as a replacement for transition metal ions in the synthesis of TiO<sub>2</sub>-based DMS. The Ce-doped ceria samples were irradiated with UV light to progressively increase the concentration of subvalent Ce<sup>3+</sup> ions. X-ray absorption near-edge structure (XANES) and extended X-ray absorption fine structure (EXAFS) techniques were employed to monitor the changes in Ce<sup>3+</sup> concentration and the number of oxygen vacancies surrounding Ce, respectively. It has been demonstrated recently that the Ce-L-edge XANES data are especially useful for studying the magnetic and catalytic properties in doped CeO<sub>2</sub> nanoparticles<sup>7,8</sup>. The variation of band gaps as a result of UV irradiation was also determined by UV-Vis diffuse reflectance measurements. Photoluminescence (PL) spectra were used to investigate the change of defect states due to UV irradiation. Finally, the magnetic property changes were experimentally observed by using a superconducting quantum interference device (SQUID) and theoretically understood by performing first-principle density functional theory (DFT) calculations.

<sup>1</sup>National Synchrotron Radiation Research Center, Hsinchu, Taiwan. <sup>2</sup>Department of Physics, National Tsing Hua University, Hsinchu, Taiwan. <sup>3</sup>Institute of Physics, Academia Sinica, Taipei, Taiwan. ✉email: soo@phys.nthu.edu.tw

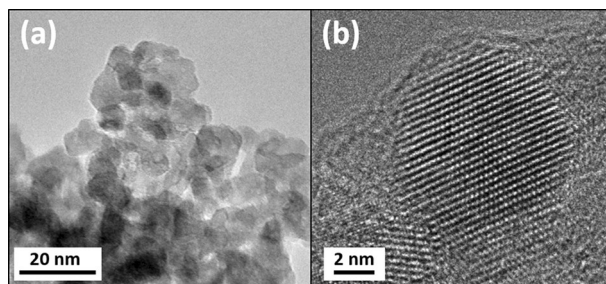


**Figure 1.** (a) Medium- and (b) high-resolution TEM images of the as-made Ce-doped TiO<sub>2</sub> samples.

## Experimental

Nanocrystal samples of Ce-doped TiO<sub>2</sub> were prepared using a sol-gel method<sup>9</sup>. As shown in Supplementary Fig. S1 online, the synchrotron-based X-ray powder diffraction pattern shows exclusively anatase TiO<sub>2</sub> Bragg peaks; no cerium oxide phase was detected. The crystallite size was determined by the Scherrer equation to be 6.4 nm. The Ce concentration was measured by inductively coupled plasma mass spectrometry (ICPMS) to be 0.98 at%. As shown in Fig. 1, the TEM images demonstrate that the Ce-doped TiO<sub>2</sub> samples have rather good crystallinity and the size of the nanoparticles is consistent with that obtained from the Scherrer equation. To study the UV-light irradiation effects, Ce-doped TiO<sub>2</sub> samples were irradiated by UV-light with various irradiation time durations in ambient condition. A handheld UVC lamp (6 W, UVGL-58, UVP) was used with an average power of 2.5 mw/cm<sup>2</sup> on the sample. After UV-light irradiation, Ce L<sub>3</sub>-edge and Ti K-edge XANES and EXAFS were performed to monitor the evolution of valances and local structures surrounding Ce and Ti atoms, respectively. All XANES and EXAFS measurements were performed in transmission mode at beamline BL07A of the Taiwan Light Source (TLS) at National Synchrotron Radiation Research Center (NSRRC). To monitor the electronic structural changes due to UV-light irradiation, the UV-Vis diffuse reflectance measurements were carried out using a spectrophotometer (UV-4150, Hitachi). Photoluminescence (PL) spectra of the as-made and irradiated samples were also measured using an excitation source of wavelength 325 nm to investigate the variation of defect states due to UV-light irradiation. Variations of the sample's magnetic properties due to UV-light irradiation were monitored by M-H and M-T measurements using a superconducting quantum interference device (SQUID).

## Results and discussion

The Ce XANES of samples with different UV-light irradiation time durations are shown in Fig. 2a. The peak ascribed to Ce<sup>3+</sup> increases with the irradiation time, representing reduction of Ce<sup>4+</sup> as a result of UV irradiation. To extract Ce<sup>3+</sup> concentration from XANES data, the spectra were curve-fitted with an arctangent function to simulate the edge jump and Gaussian functions for peak features. Details of the curve-fitting method have been previously reported<sup>10</sup>. It's worth noting that application of Ce-L-edge XANES on the studies of magnetism and photocatalysis in doped CeO<sub>2</sub> has also been reported recently<sup>7,8</sup>. As shown in Fig. 2b, after 600 min of UV-light irradiation, the Ce<sup>3+</sup> concentration increased from 23.9% and saturated at 68.6%. Figure 2c shows the Ti XANES of the samples before and after UV-light irradiation. Notably, despite the dramatic changes observed in Ce XANES, the Ti XANES showed the same spectrum even after 600 min of UV-light irradiation, representing an unchanged or at most marginally affected Ti valence state.

The Ce L<sub>3</sub>-edge and Ti K-edge EXAFS analyses were also performed using the ARTEMIS package<sup>11</sup> to probe the local structural variations due to UV-light irradiation surrounding the Ce dopant atoms and Ti constituent atoms, respectively, in Ce-doped TiO<sub>2</sub>. As shown in Fig. 3a and Supplementary Table S1 online, the as-made sample has one O shell at 2.13 ± 0.01 Å and a Ti shell at 3.18 ± 0.02 Å from the Ce central atom, with coordination numbers 5.7 ± 0.5 and 3.4 ± 0.3, respectively. The Ce-O bond length of 2.13 Å observed in the as-made sample is substantially shorter than that of 2.34 Å in the fluorite ceria structure. However, except for longer interatomic distances due to larger ionic radius of Ce<sup>4+</sup> (87 pm) compared to that of Ti<sup>4+</sup> (61 pm), the local structural parameters for Ce in the as-made sample resemble those for Ti in TiO<sub>2</sub>, in which 6 O atoms and 4 Ti atoms are located at 1.95 Å and 3.04 Å from the central Ti central atom, respectively. We therefore conclude that the Ce dopant atoms in the as-made Ce-doped TiO<sub>2</sub> sample are most likely substitutionally incorporated into the host matrix, occupying Ti sites in TiO<sub>2</sub>. After 600 min of UV-light irradiation, as listed in Supplementary Table S1 online, the coordination number of the (O) nearest neighboring shell is reduced from 5.7 to 3.8, representing the formation of O vacancy surrounding the Ce dopant atoms as a result of UV irradiation. This is consistent with the Ce XANES results that Ce<sup>4+</sup> is reduced to Ce<sup>3+</sup> due to UV-light-induced Ce-O bond breakage in the irradiated sample.

In contrast to the Ce local structure which can be substantially changed by UV irradiation, the local structure surrounding Ti atoms appears to remain largely intact after 600 min of UV-light irradiation. As shown in Fig. 3b, the Fourier transform of the Ti EXAFS  $\chi$ -function for the irradiated sample generally resembles that for the as-made sample. Within fitting uncertainties, the final values of the local structural parameters obtained from curve-fittings for the irradiated samples are also unchanged from those for the as-made samples (Supplementary Table S2 online). Therefore, our EXAFS analysis is consistent with the XANES results that UV irradiation changes the local chemical environment surrounding Ce dopant atoms without inducing substantial variation to that surrounding Ti constituent atoms in the TiO<sub>2</sub> host.

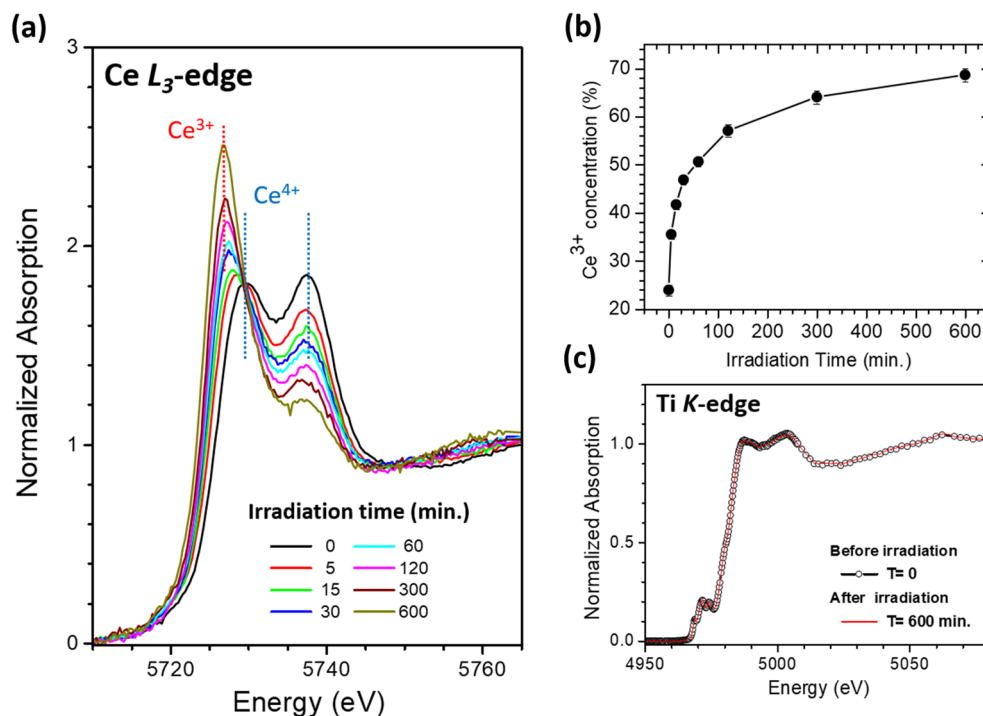


**Figure 2.** (a) Ce  $L_3$ -edge XANES of UV-light irradiated sample with various irradiation times. (b) Plot of  $Ce^{3+}$  concentration vs. irradiation time. (c) Ti K-edge XANES of sample before and after 600 min of UV-light irradiation.

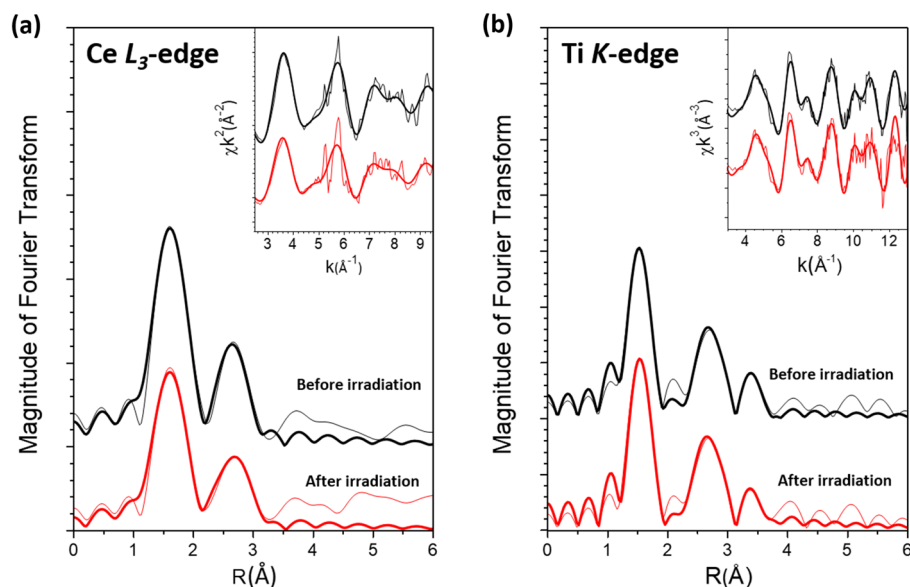


**Figure 3.** (a) Ce  $L_3$ -edge and (b) Ti K-edge EXAFS data for the sample before and after 600 min of UV-light irradiation. Fine lines: experimental; Coarse lines: curve fitting. Curves have been shifted vertically for the sake of clarity.

The band gap values of the as-made sample and the samples irradiated for different time durations were extracted from the UV-Vis diffuse reflectance data using the Kubelka-Munk function<sup>12</sup> and Tauc's plots<sup>13</sup> as shown in Fig. 4. The 2.8 eV ( $E_g$ ) band gap value for the as-made sample is smaller than the reported 3.2 eV indirect band gap of anatase  $TiO_2$ <sup>14</sup>. According to the DFT calculations published by Albuquerque et al.<sup>15</sup>, the  $Ce^{4+}$  ( $4f^0$ ) band for Ce dopant atoms deep in bulk  $TiO_2$  completely overlaps with the Ti 3d band while those for the subsurface and surface Ce atoms are just below and well below the Ti 3d states, respectively. The observed

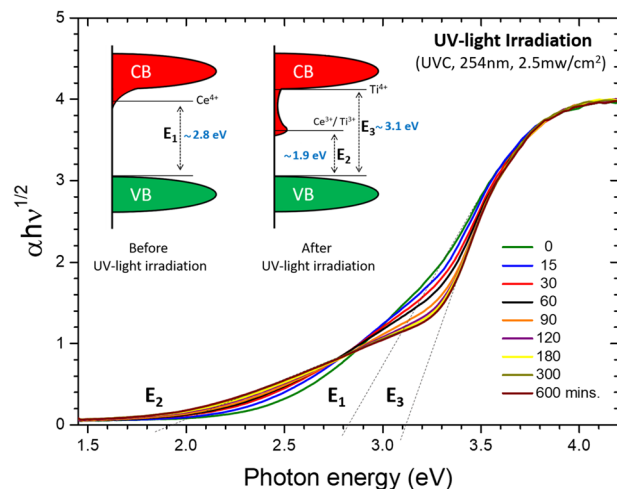


**Figure 4.** Plot of  $(\alpha hv)^{1/2}$  vs.  $h\nu$  deduced from the UV-Vis diffuse reflectance spectra of UV-light irradiated sample with various irradiation times.

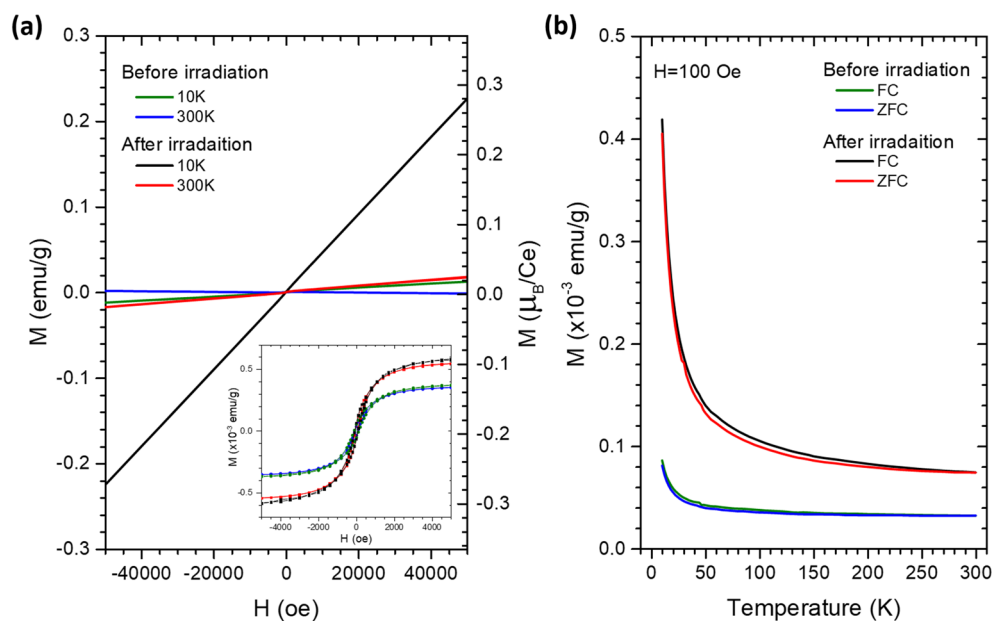


**Figure 5.** (a) M-H curves and (b) FC/ZFC curves of Ce-doped  $\text{TiO}_2$  sample before and after 600 min of UV-light irradiation. The inset of (a) shows the ferromagnetic component of each curve obtained by subtracting the paramagnetic background from the original curve.

band-gap narrowing is ascribed to the presence of a  $\text{Ce}^{4+}$  impurity band in the energy gap that extends past the conduction band minimum of  $\text{TiO}_2$  due to Ce doping.

For the UV-light irradiated sample, it was observed that a band-tailing effect progressively emerged with increase in irradiation time. As shown in Fig. 4, the initially smooth  $(\alpha hv)^{1/2}$  vs.  $h\nu$  curve is gradually lowered in the region from 2.8 to 3.4 eV and raised in that from 1.9 to 2.8 eV due to UV-light irradiation. Consequently, the energy band gap  $E_1$  for the as-made sample gradually split into a smaller gap  $E_2$  and a larger gap  $E_3$  as the irradiation time increases. As revealed by previous DFT calculations and X-ray measurements, the  $\text{Ti}^{3+}$  and  $\text{Ce}^{3+}$  defect states spawned by UV-light irradiation formed conduction band tail states that extend into the energy band gap and decreases the band gap value<sup>15,16</sup>. After 600 min of UV irradiation, the band gap value decreased to 1.9 eV ( $E_2$ ). As a consequence of the  $\text{Ce}^{4+}$  to  $\text{Ce}^{3+}$  conversion, an additional higher band gap of 3.1 eV ( $E_3$ ) was also observed, which can be attributed to the valance band to  $\text{Ti}^{4+}$  transition.

The effects of UV-light irradiation on the sample's magnetic properties were monitored by SQUID measurements. As revealed in Fig. 5, the M-H curve of the as-made sample exhibits a combination of ferromagnetism and paramagnetism up to room temperatures. After UV-light irradiation, the magnetization in the sample was

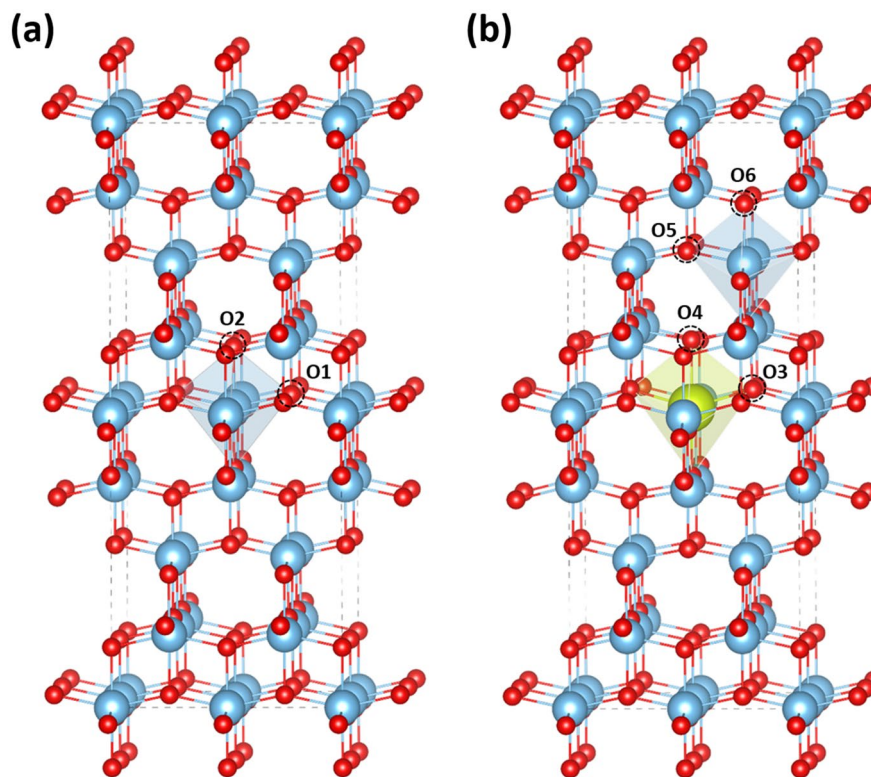


**Figure 6.** Schematic view of undoped and Ce-doped anatase  $\text{TiO}_2$ . **(a)** The possible O vacancy sites  $V_{O1}$  and  $V_{O2}$  in a  $[\text{TiO}_6]$  octahedron of the undoped  $\text{TiO}_2$ . Note that  $V_{O1}$  and  $V_{O2}$  are symmetrically equivalent in the crystal structure of  $\text{TiO}_2$ . **(b)** The possible O vacancy sites  $V_{O3}$ ,  $V_{O4}$ ,  $V_{O5}$ , and  $V_{O6}$  of the Ce-doped  $\text{TiO}_2$ . Vacancies sites  $V_{O3}$ ,  $V_{O4}$  are in a  $[\text{CeO}_6]$  octahedron, whereas  $V_{O5}$  and  $V_{O6}$  sites are in the next-nearest-neighboring  $[\text{TiO}_6]$  octahedron. The large blue balls, large green balls, and small red balls represent the Ti, Ce, and O atoms, respectively. The  $[\text{TiO}_6]$  and  $[\text{CeO}_6]$  octahedrons are shown in blue and green, respectively. This figure was drawn by using the VESTA 3 software<sup>20</sup>. <https://jp-minerals.org/vesta/en/download.html>.

substantially increased compared to that in the as-made sample. The field cooled (FC) and zero field cooled (ZFC) magnetization measurements under an applied field of 200 Oe also show enhanced magnetization due to UV-light irradiation up to the temperature of 300 K.

### Theoretical calculations

To explain the observed enhancement of magnetic properties of Ce-doped  $\text{TiO}_2$  due to UV-light irradiation, spin-polarized DFT calculations using VASP codes were employed to estimate the formation energies of O vacancy defects on different sites<sup>17</sup>. The projector augmented-wave (PAW) method and the generalized gradient approximation (GGA) within the parameterization of Perdew–Burke–Ernzerhof (PBE) were used in the calculation<sup>18</sup>. The Ce ( $5s^25p^66s^24f^15d^1$ ), Ti ( $3p^64s^23d^2$ ) and O ( $2s^22p^4$ ) electrons were treated as valence electrons and their state functions were expanded on a plane-wave basis with a kinetic energy cutoff of 500 eV. A GGA + U method was used for the correction of on-site Coulomb interactions with  $U = 4$  eV applied to both the Ce 4f- and Ti 3d-states. As reported previously, an accumulation of positive charge was observed on the  $\text{TiO}_2$  surface during UV-light irradiation<sup>19</sup>. Different numbers of valence electrons were removed from the supercell in our calculation to mimic the creation of valence holes during UV-light irradiation. The initial structural model used for the DFT calculation was constructed from a  $2 \times 2 \times 2$  supercell of anatase  $\text{TiO}_2$ . To construct the structural model for Ce-doped  $\text{TiO}_2$ , one Ti atom was replaced by a Ce atom in the 96-atom supercell, resulting in a  $\text{Ti}_{0.97}\text{Ce}_{0.03}\text{O}_2$  stoichiometry (3.1% Ce).

Oxygen vacancy defects on different sites in  $\text{TiO}_2$  and Ce-doped  $\text{TiO}_2$  are also considered in the structural model. As shown in Fig. 6a, an O atom was removed from either the O1 or O2 site of the  $[\text{TiO}_6]$  octahedron in the undoped  $\text{TiO}_2$  model. We note that the O1 and O2 sites are symmetrically equivalent in the crystal structure of  $\text{TiO}_2$ . On the other hand, one of the O vacancies on the O3 and O4 sites of the  $[\text{CeO}_6]$  octahedron and the O5 and O6 sites of the  $[\text{TiO}_6]$  octahedron was created for each defective Ce-doped  $\text{TiO}_2$  model as shown in Fig. 6b. Geometry optimization was carried out for all structural models with a  $5 \times 5 \times 3$  Monkhorst–Pack k-point grid. The atomic coordinates and the lattice parameters were optimized until the maximum force on each atom was less than  $0.02 \text{ eV}/\text{\AA}$  with an electronic self-consistency convergence of  $10^{-6} \text{ eV}$ . The spin density isosurfaces are shown in Fig. 7, corresponding to the trapped electrons that lead to the defect levels in the energy gap. While the electron spin densities for defect states near oxygen vacancies  $V_{O1}$  in pure  $\text{TiO}_2$  are in antiferromagnetic

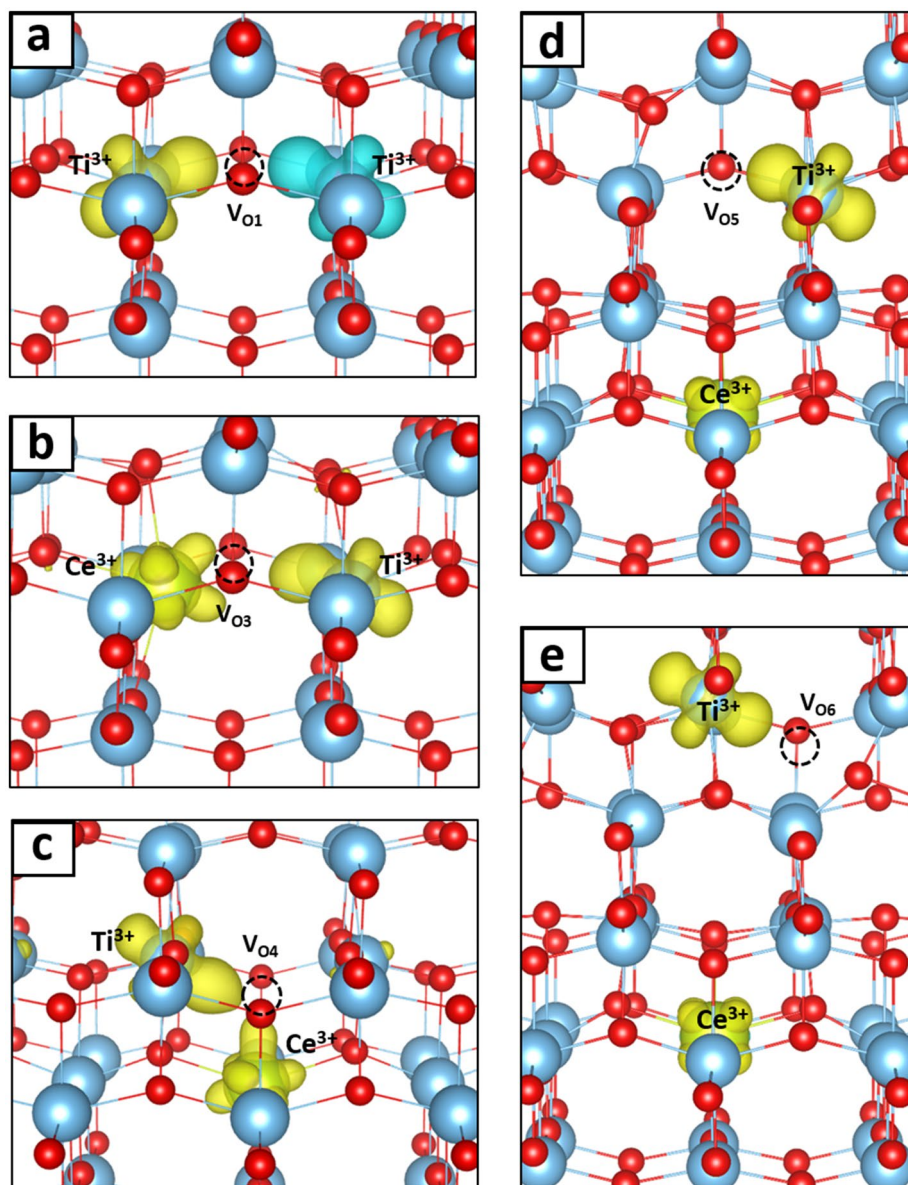


**Figure 7.** Structure and spin density isosurface of (a) oxygen vacancy  $V_{O1}$ , (b) oxygen vacancy  $V_{O3}$ , (c) oxygen vacancy  $V_{O4}$ , (d) oxygen vacancy  $V_{O5}$ , and (e) oxygen vacancy  $V_{O6}$ . The  $\alpha$  and  $\beta$  spin densities are shown in yellow and blue, respectively. See text for a more detailed description of the different structures. Isosurface:  $0.006 \text{ e}^-/\text{\AA}^3$ . This figure was drawn by using the VESTA 3 software<sup>20</sup>. <https://jp-minerals.org/vesta/en/download.html>.

orientation, they are in ferromagnetic orientations near oxygen vacancies  $V_{O3}$ ,  $V_{O4}$ ,  $V_{O5}$ , and  $V_{O6}$  in Ce-doped  $\text{TiO}_2$ , as indicated in Fig. 7. Therefore, if oxygen vacancies can be created by UV irradiation in the Ce-doped  $\text{TiO}_2$  samples, the ferromagnetically oriented spin densities near such oxygen vacancies are likely responsible for the experimentally observed enhancement of magnetism in the UV irradiated samples of Ce-doped  $\text{TiO}_2$ .

To elucidate the possible mechanism for creation of oxygen vacancies by UV irradiation in the pure and Ce-doped samples of  $\text{TiO}_2$ , the formation energies of O vacancy  $E_{VO}^F$  were obtained as the difference in total energies between two supercells using the following equation:

$$E_{VO}^F(q) = E_T(\text{Ce}_n\text{Ti}_{32-n}\text{O}_{63}, q) - E_T(\text{Ce}_n\text{Ti}_{32-n}\text{O}_{64}, q) + \frac{1}{2}E_T(\text{O}_2)$$

where  $E_T(\text{Ce}_n\text{Ti}_{32-n}\text{O}_{63}, q)$  and  $E_T(\text{Ce}_n\text{Ti}_{32-n}\text{O}_{64}, q)$  are the total energies of the optimized supercells with and without an O vacancy, respectively,  $q$  is the number of electrons removed from the supercell by UV irradiation, and  $E_T(\text{O}_2)$  is the total energy for the ground triplet state of an optimized oxygen molecule in the gas phase.

The oxygen vacancy formation energies in all defect structures discussed above are summarized in Supplementary Table S3 online. In the pure TiO<sub>2</sub> model, although the Ti–O<sub>1</sub> and Ti–O<sub>2</sub> bonds in a [TiO<sub>6</sub>] octahedron have different bond lengths, the two O atoms O<sub>1</sub> and O<sub>2</sub> are symmetrically equivalent in the crystal structure and therefore the O vacancy formation energy for both sites have the same value of 4.98 eV. As shown in Fig. 7a, when an O atom is removed from TiO<sub>2</sub>, the two electrons left in the O vacancy are transferred to the two nearest Ti atoms, forming Ti<sup>3+</sup> defect states in an antiferromagnetic orientation. In the presence of a valence hole created by UV-light irradiation, only one electron is transferred and the Coulomb energy of the system is thus largely lowered. The O vacancy formation energy is therefore lowered to 2.51 eV. When there are two valence holes, the O vacancy formation energy is further lowered to 0.43 eV.

In the Ce-doped TiO<sub>2</sub> model, with a Ce atom on the octahedral Ti site, the O atoms surrounding Ce in the [CeO<sub>6</sub>] octahedron are not symmetrically equivalent. Therefore, the O vacancies at the O3 and O4 sites of the [CeO<sub>6</sub>] octahedron are considered separately. For O atom removal from the O3 site and the O4 site shown in Fig. 7b,c, respectively, the two electrons left in the O vacancy will be transferred to the Ce atom and the nearest Ti atom, forming Ce 4f and Ti 3d defect states in a ferromagnetic orientation for both cases. In comparison to the V<sub>O3</sub> structure, only a small structural relaxation is observed in the V<sub>O4</sub> structure, leading to a higher O vacancy formation energy of 4.64 eV at the O4 site than that of 4.08 eV at the O3 site. Therefore, the V<sub>O3</sub> structure is energetically favored compared to the V<sub>O4</sub> structure. In the presence of a valence hole generated by UV-light irradiation, only one electron is left in the Ce 4f state. The O vacancy formation energies at the O3 and O4 sites decreased to 0.95 eV and 2.30 eV, respectively. When two valence holes are created, their O vacancy formation energies are further lowered to –0.74 eV and 0.42 eV, representing the onset of an O vacancy formation at the O3 site. We therefore have theoretically demonstrated the Ce reduction mechanism induced by valence-hole-generating UV-light irradiation. Finally, when an oxygen atom is removed from the O5 or O6 sites, the two electrons left will be transferred to the nearest Ti atom and the Ce atom, forming Ti<sup>3+</sup> and Ce<sup>3+</sup> defect states in ferromagnetic orientations as demonstrated in Fig. 7d,e. The formation energies of O5, O6 oxygen vacancies were calculated to be 4.86 eV and 4.82 eV, respectively. As the UV irradiation generated one and two valence holes, the formation energies were reduced to 2.56 eV and 0.51 eV for the O5 vacancy and 2.57 eV and 0.51 eV for the O6 vacancy, respectively. It is worth noting that the formation of the oxygen vacancies in the sample is followed by the relaxation of the UV-generated valence holes, leaving the Ce dopant ions in their reduced valence state as is incorporated into the magnetic calculations above.

To summarize the theoretical results, we note that the formation of oxygen vacancies at the O3 sites in the supercells of the Ce-doped TiO<sub>2</sub> structure is energetically favorable and thus tends to occur when two electrons are removed from each supercell of the crystal by UV irradiation. Our calculations also indicate that the electron spin densities for defect states near V<sub>O3</sub> are in ferromagnetic orientations. Therefore, we have theoretically demonstrated that UV irradiation can generate oxygen vacancies near Ce dopant atoms with electron spin densities in ferromagnetic orientations, leading to the experimentally observed reduction of Ce and enhancement of magnetic properties in Ce-doped TiO<sub>2</sub>.

## Conclusion

We experimentally observed generation of oxygen vacancy defects and consequent reduction of Ce in Ce-doped TiO<sub>2</sub> diluted magnetic semiconductor samples as a result of UV-light irradiation by using synchrotron radiation X-ray techniques including XANES and EXAFS. The variation of electronic states observed by UV-Vis diffuse reflectance and photoluminescence measurements also shows reduction of Ce and oxygen vacancy generation in the samples due to UV irradiation. The increase of oxygen vacancies led to substantially enhanced room-temperature ferromagnetism as demonstrated by our SQUID results. The formation of oxygen vacancy defects and enhancement of magnetism were also theoretically explained by our first-principle DFT calculations. Cerium-doped TiO<sub>2</sub> diluted magnetic semiconductors with room-temperature ferromagnetism enhanced by UV-light irradiation are potentially useful for many technological applications.

## Methods

Nanocrystal samples of Ce-doped TiO<sub>2</sub> were prepared using a sol-gel method. The crystal structures and particle sizes of the samples were obtained from synchrotron-based XRD using the Scherrer equation. Coupled plasma mass spectrometry (ICPMS) measurements were employed to determine the Ce concentration of the samples. The Ce-doped TiO<sub>2</sub> samples were then irradiated by UV-light from a UVC lamp (6 W, UVGL-58, UVP) with various irradiation time durations in ambient conditions. The Ce L<sub>3</sub>-edge and Ti K-edge XANES and EXAFS, performed at beamline BL07A of the Taiwan Light Source (TLS) at National Synchrotron Radiation Research Center (NSRRC), were used to reveal the evolution of valences and local structures surrounding Ce and Ti atoms as a result of UV irradiation, respectively. Electronic structural changes due to UV-light irradiation were monitored by UV-Vis diffuse reflectance measurements using a spectrophotometer (UV-4150, Hitachi). Photoluminescence (PL) spectra were also measured using an excitation source of wavelength 325 nm to investigate the variation of defect states due to UV-light irradiation. The UV-induced magnetic-property changes were exhibited by the M–H and M–T data obtained by using a superconducting quantum interference device (SQUID). Finally, the experimentally observed effects of UV irradiation on Ce-doped TiO<sub>2</sub> were theoretically explained by first-principle DFT calculations using the VASP code.

## Data availability

All data generated or analyzed during this study are included in the main text and supplementary information of this published article.

Received: 9 November 2020; Accepted: 22 March 2021

Published online: 07 April 2021

## References

- Hong, N. H. *et al.* Ferromagnetism in transition-metal-doped TiO<sub>2</sub> thin films. *Phys. Rev. B* **70**, 195204 (2004).
- Janisch, R., Gopal, P. & Spaldin, N. A. Transition metal-doped TiO<sub>2</sub> and ZnO—Present status of the field. *J. Phys. Condens. Matter* **17**, R657 (2005).
- Tian, J. *et al.* Influence of transition metal doping on the structural, optical, and magnetic properties of TiO<sub>2</sub> films deposited on Si substrates by a sol–gel process. *Nanosci. Res. Lett.* **8**, 533 (2013).
- Tseng, L.-T. *et al.* Structures and properties of transition-metal-doped TiO<sub>2</sub> nanorods. *Mater. Lett.* **170**, 142–146 (2016).
- Kim, J.-Y. *et al.* Ferromagnetism induced by clustered Co in Co-doped anatase TiO<sub>2</sub> thin films. *Phys. Rev. Lett.* **90**, 017401 (2003).
- Kang, Y. *et al.* Room-temperature magnetism of ceria nanocubes by inductively transferring electrons to Ce atoms from nearby oxygen vacancy. *Nano-Micro Lett.* **8**, 13–19 (2016).
- Ranjith, K. S. *et al.* Enhanced room-temperature ferromagnetism on Co-doped CeO<sub>2</sub> nanoparticles: Mechanism and electronic and optical properties. *Phys. Chem. C* **118**, 27039–27047 (2014).
- Ranjith, K. S. *et al.* Evolution of visible photocatalytic properties of Cu-doped CeO<sub>2</sub> nanoparticles: Role of Cu<sup>2+</sup>-mediated oxygen vacancies and the mixed-valence states of Ce ions. *ACS Sustain. Chem. Eng.* **6**, 8536–8546 (2018).
- Yan, N., Zhu, Z., Zhang, J., Zhao, Z. & Liu, Q. Preparation and properties of ce-doped TiO<sub>2</sub> photocatalyst. *Mater. Res. Bull.* **47**, 1869–1873 (2012).
- Wu, T. S. *et al.* Enhancement of catalytic activity by UV-light irradiation in CeO<sub>2</sub> nanocrystals. *Sci. Rep.* **9**, 8018 (2019).
- Ravel, B. & Newville, M. ATHENA, ARTEMIS, HEPHAESTUS: Data analysis for X-ray absorption spectroscopy using IFEFFIT. *J. Synchrotron Rad.* **12**, 537–541 (2005).
- Kubelka, P. & Munk, F. Ein Beitrag zur. *Optik der Farbenstriche. Z. Tech. Phys. (Leipzig)* **12**, 593–601 (1931).
- Tauc, J. & Menth, A. States in the gap. *J. Non-Cryst. Solids* **8**, 569–585 (1972).
- Zhu, T. & Gao, S. P. The stability, electronic structure, and optical property of TiO<sub>2</sub> polymorphs. *J. Phys. Chem. C* **118**, 11385–11396 (2014).
- Albuquerque, A. R., Bruix, A., Sambrano, J. R. & Illas, F. Theoretical study of the stoichiometric and reduced Ce-doped TiO<sub>2</sub> Anatase (001) surfaces. *J. Phys. Chem. C* **119**, 4805–4806 (2015).
- Albuquerque, A. R., Bruix, A., Santos, I. M. G., Sambrano, J. R. & Illas, F. DFT study on Ce-doped anatase TiO<sub>2</sub>: Nature of Ce<sup>3+</sup> and Ti<sup>3+</sup> centers triggered by oxygen vacancy formation. *J. Phys. Chem. C* **118**, 9677–9689 (2014).
- Kresse, G. & Furthmüller, J. Efficient iterative schemes for ab initio total-energy calculations using a plane-wave basis set. *Phys. Rev. B* **54**, 11169 (1996).
- Perdew, J. P., Burke, K. & Ernzerhof, M. Generalized gradient approximation made simple. *Phys. Rev. Lett.* **77**, 3865 (1996).
- Stevanovic, A., Büttner, M., Zhang, Z. & Yates, J. T. Jr. Photoluminescence of TiO<sub>2</sub>: Effect of UV light and adsorbed molecules on surface band structure. *J. Am. Chem. Soc.* **134**, 324–332 (2012).
- Momma, K. & Izumi, F. VESTA 3 for three-dimensional visualization of crystal, volumetric and morphology data. *J. Appl. Crystallogr.* **44**, 1272–1276 (2011).

## Author contributions

T.S.W. and Y.L.S. conceived and designed the experiments. T.S.W. prepared the materials. T.S.W., L.Y.S., S.C.W., Y.S.H. and Y.L.S. planned and performed the synchrotron radiation X-ray measurements. T.S.W. and B.H.L. performed the PL measurements. T.S.W. and H.T.J. performed the DFT calculations. T.S.W. and Y.L.S. co-wrote the paper.

## Funding

Funding was provided by Ministry of Science and Technology, Taiwan (Grant Number: 107-2112-M-007-027-MY3).

## Competing interests

The authors declare no competing interests.

## Additional information

**Supplementary Information** The online version contains supplementary material available at <https://doi.org/10.1038/s41598-021-87115-z>.

**Correspondence** and requests for materials should be addressed to Y.-L.S.

**Reprints and permissions information** is available at [www.nature.com/reprints](http://www.nature.com/reprints).

**Publisher's note** Springer Nature remains neutral with regard to jurisdictional claims in published maps and institutional affiliations.



**Open Access** This article is licensed under a Creative Commons Attribution 4.0 International License, which permits use, sharing, adaptation, distribution and reproduction in any medium or format, as long as you give appropriate credit to the original author(s) and the source, provide a link to the Creative Commons licence, and indicate if changes were made. The images or other third party material in this article are included in the article's Creative Commons licence, unless indicated otherwise in a credit line to the material. If material is not included in the article's Creative Commons licence and your intended use is not permitted by statutory regulation or exceeds the permitted use, you will need to obtain permission directly from the copyright holder. To view a copy of this licence, visit <http://creativecommons.org/licenses/by/4.0/>.

© The Author(s) 2021